Extreme Mechanics Letters 42 (2021) 101132

Contents lists available at ScienceDirect

Extreme Mechanics Letters

journal homepage: www.elsevier.com/locate/eml

A mechanical model of blastocyst hatching

Viggo Tvergaard [a], Daniel Needleman [b,c], Alan Needleman [d,*]

[a] Department of Mechanical Engineering, The Technical University of Denmark, Lyngby, Denmark
[b] Department of Molecular and Cellular Biology and School of Engineering and Applied Sciences, Harvard University, Cambridge, MA, United States of America
[c] Center for Computational Biology, Flatiron Institute, New York, NY, United States of America
[d] Department of Materials Science & Engineering, Texas A&M University, College Station, TX, United States of America

ARTICLE INFO

Article history:
Received 15 September 2020
Received in revised form 30 November 2020
Accepted 2 December 2020
Available online 8 December 2020

Keywords:
Mammalian embryo hatching
Shell mechanics
Pressure loading

ABSTRACT

We develop a continuum mechanics model of blastocyst hatching. The blastocyst and the zona pellucida are modeled as concentric thick-walled initially spherical shells embedded in a viscous medium. Each shell is characterized by a nonlinear elastic–viscous–constitutive relation. The stiffer outer shell (the zona pellucida) contains an opening. The softer inner shell (the blastocyst) is subject to a continually increasing pressure, which can eventually drive the escape of the inner shell from the outer shell ("hatching"). The focus is on the continuum mechanics modeling framework and illustrating the sort of quantitative predictions that can be made. Numerical examples are presented for the predicted dependence of the evolution of the escape process on values of parameters characterizing the constitutive response of the shells, on the viscosity of the external medium and on the size of the opening in the zona pellucida.

1. Introduction

Mammalian oocytes (immature eggs) are surrounded by a glycoprotein hydrogel called the zona pellucida [1–3]. After fertilization, the early embryo initially develops inside the zona pellucida, but ultimately must hatch out of the zona pellucida in order to implant into the uterine wall. Escape of the embryo from the zona pellucida is believed to involve both chemical and mechanical processes. Chemically, the embryo secretes enzymes that degrade the zona pellucida. Mechanically, the embryo, called a blastocyst at this stage, actively pumps ions into an intercellular space (the blastocele) [4,5]. The resulting osmotic pressure causes the blastocele to grow larger, and the blastocyst can eventually exit through an opening in the degrading zona pellucida. In vitro fertilization (IVF) clinics often perform an "assisted hatching" procedure that aims to help the blastocyst hatch by creating an opening in the zone pellucida [6]. After successful hatching the blastocyst implants into the lining of the uterus so that the embryo can continue to develop. However, hatching is not always successful.

Despite the importance of hatching, from the perspectives of both fundamental developmental biology and clinical IVF, the process remains poorly understood. Here, we develop an idealized continuum mechanics model of blastocyst hatching. The blastocyst/zona pellucida structure is modeled as consisting of two concentric shells with the inner shell being the blastocyst and the outer shell the zona pellucida. The blastocyst/zona pellucida structure is subject to a monotonically increasing internal pressure. The two shells are connected by linear compressive springs along their interface. The outer shell (the zona pellucida) has an opening through which hatching takes place. The effect of the surrounding viscous medium is idealized by a body force that is proportional to the material velocity. Full dynamic, finite deformation finite element calculations are carried out with the deformations constrained to remain axisymmetric. Although it is expected, and computational results verify, that material inertia plays a negligible role, the dynamic formulation is computationally convenient and reasonably efficient. Numerical examples illustrate the sort of quantitative predictions that can be obtained.

2. Problem formulation

2.1. Initial/boundary value problem

The blastocyst/zona pellucida structure is modeled as two concentric thick-walled initially spherical shells in a viscous fluid with a monotonically increasing internal pressure. The inner shell, the blastocyst, is relatively soft while the outer shell, the zona pellucida, is stiffer. The two shells are taken to be in contact initially and are free to slide over each other. The configuration analyzed is shown in Fig. 1.

* Corresponding author.
E-mail address: needle@tamu.edu (A. Needleman).

https://doi.org/10.1016/j.eml.2020.101132
2352-4316/

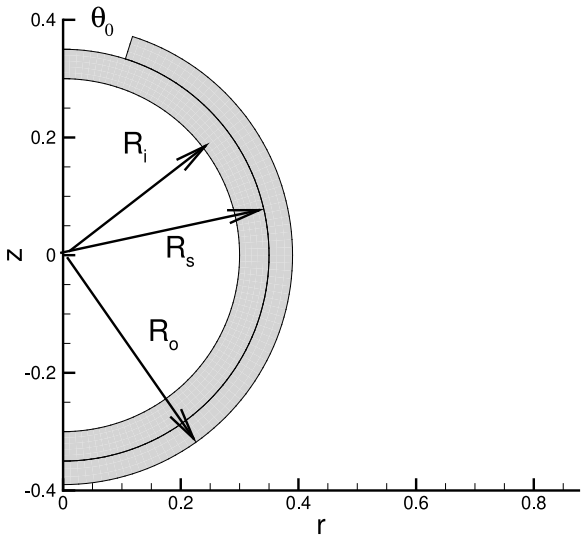

Fig. 1. Sketch of the configuration analyzed. The blastocyst and zona pellucida are each modeled as an initially spherical shell, with R_i the inner radius of the blastocyst, R_s the interface radius, R_o is the outer radius of the zona pellucida and θ_0 characterizes the opening in the zona pellucida.

The calculations of the deformation histories are carried out using a Lagrangian finite deformation convected coordinate formulation for a three dimensional solid with the restriction that the deformations are axisymmetric. Material points are identified by their positions (y^1, y^2, y^3) in the initial, stress free, configuration with the identification in polar coordinates of $y^1 = r$, $y^2 = \phi$ and $y^3 = z$. Due to the axisymmetry all field quantities are independent of ϕ.

The internal pressure is applied on the inner surface $r = R_i$, the boundary between the two shells on which sliding occurs is at $r = R_s$ and the outer radius is R_o. The opening in the outer spherical shell (the zona pellucida) is presumed to be present at the initiation of pressure loading and the size of the opening is identified by the angle θ_0 from the z-axis in the initial configuration as shown in Fig. 1.

The material point initially at $\mathbf{X}$ in the reference configuration is at $\mathbf{x}$ in the current configuration. The displacement vector $\mathbf{u}$ and the deformation gradient $\mathbf{F}$ are then defined by

$$\mathbf{u} = \mathbf{x} - \mathbf{X} \quad , \quad \mathbf{F} = \frac{\partial \mathbf{x}}{\partial \mathbf{X}} \tag{1}$$

Modeling the interaction between the two shells, the blastocyst and the zona pellucida and the surrounding fluid is a complex fluid–structure interaction problem. Here, the effect of the interaction of the surrounding fluid on the shells is modeled as a viscous body force $\mathbf{f}_v$. The finite element calculations are based on the principle of virtual work which is written in the reference configuration in the form.

$$\int_V \mathbf{s} : \delta\mathbf{F} dV + \int_V \mathbf{f}_v \cdot \delta\mathbf{u} dV - \int_{S_s} \mathbf{T} \cdot \delta[\mathbf{u}] dS$$
$$= -\int_{S_p} p\boldsymbol{\alpha} \cdot \mathbf{n} \cdot \delta\mathbf{u} dS - \int_V \rho \frac{\partial^2 \mathbf{u}}{\partial t^2} \cdot \delta\mathbf{u} dV \tag{2}$$

Here, $(\cdot)$ denotes the vector inner product, $(:)$ denotes the second order tensor inner product, t is time, $\mathbf{s}$ is the (unsymmetric) nominal stress tensor, $\mathbf{s} = \mathbf{F}^{-1} \cdot \boldsymbol{\tau}$ with the Kirchhoff stress $\boldsymbol{\tau} = (\det \mathbf{F})\boldsymbol{\sigma}$ where $\boldsymbol{\sigma}$ is the Cauchy stress, $\mathbf{f}_v$ is a viscous body force and ρ is the mass density. The material volume in the reference configuration V is the sum of the volume of the inner shell (the blastocyst) V_i and the volume of the outer shell (the zona pellucida) V_o, S_p is the surface $r = R_i$ in the reference configuration where pressure is applied, p is the pressure and $\boldsymbol{\alpha} = \det(\mathbf{F})\mathbf{F}^{-T}$ where $\mathbf{F}^{-T}$ is the inverse of the transpose of $\mathbf{F}$ and $\mathbf{n}$ is the normal to S_p. The surface S_s, given in the reference configuration by $r = R_s$, is the surface where sliding of the inner shell (the blastocyst) occurs along the outer shell (the zona pellucida) during hatching, $\mathbf{T}$ is a traction introduced along $r = R_s$ to inhibit interpenetration of the two shells and $[\mathbf{u}]$ is the displacement jump along $r = R_s$. During hatching the surface S_s changes as the inner shell (the blastocyst) separates from the outer shell (the zona pellucida).

The viscous body force used to represent friction between the fluid and the material that occurs as water passes through the surface of the expanding blastocyst and is taken to be proportional to the velocity vector $\mathbf{v} = \partial\mathbf{u}/\partial t$ at a fixed material point, so that

$$\mathbf{f}_v = c\mathbf{v} \tag{3}$$

It is expected that the viscous force associated with the external medium is much larger than the material inertia force. However, the inertia term stabilizes the calculations so that the value of density ρ is chosen to maintain numerical stability while having a small effect on the results (larger values of ρ lead to more stable calculations). Thus, the density ρ is regarded as a parameter of the numerical implementation rather than as being representative of the actual material density.

The shells representing the blastocyst and the zona pellucida are taken to be in contact initially although there may be a thin liquid layer separating them. The spring force penalizes interpenetration and acts in the direction of the current normal to the surface $r = R_s$. It is convenient to calculate this term in the current configuration, so that

$$\int_{S_s} \mathbf{T} \cdot \delta[\mathbf{u}] dS = \int_{\bar{S}_s} \bar{T}_{\bar{n}} \delta[\bar{u}]_{\bar{n}} d\bar{S} \tag{4}$$

where $\bar{T}_{\bar{n}} = \bar{\mathbf{T}} \cdot \bar{\mathbf{n}}$ and $[\bar{u}]_{\bar{n}} = [\bar{u}] \cdot \bar{\mathbf{n}}$ and a superposed bar denotes quantities in the current configuration.

The traction, $\bar{T}_{\bar{n}}$, is related to the displacement jump, $[\bar{u}]_{\bar{n}}$, via

$$\bar{T}_{\bar{n}} = \begin{cases} \pm K \dfrac{[\bar{u}]_{\bar{n}}}{\delta_n} & [\bar{u}]_{\bar{n}} \le 0 \\ 0 & [\bar{u}]_{\bar{n}} > 0 \end{cases} \tag{5}$$

The spring stiffness is essentially a penalty parameter and, as for any penalty method, if the value of the penalty parameter, K/δ_n in Eq. (5) is taken to be too large, the calculation becomes numerically unstable. If the value of K/δ_n is taken to be too small, significant overlap of the inner shell (the blastocyst) and the outer shell (the zona pellucida) occurs. The choice of an appropriate value of K/δ_n is problem dependent. An alternative approach would be to enforce the constraint $[\bar{u}]_{\bar{n}} = 0$ directly. A few calculations were carried out exploring the use of this constraint on part of the interface where $[\bar{u}]_{\bar{n}} < 0$. This had a small effect on the results and did not significantly improve the numerical stability. In addition, the coding to enforce this constraint in general is more complex, so the results to be presented were obtained using the penalty approach of Eq. (5). It is also worth noting that our framework can be modified to account for more complex interface descriptions and to include tangential as well as normal components.

The finite element implementation follows that in Refs. [7] and [8]. For the stress work term, the first volume integral on the left hand side of Eq. (2), eight node quadratic elements are used with four point Gauss integration. The evaluation of the body force and inertia volume integrals also use eight node quadratic elements but with nine point Gauss integration. The integration

along the surface S_p is carried out using four point Gauss integration in each surface element. On the other hand, three point Gauss integration is used in the deformed configuration along the interface surface $\bar{S}_s$ in Eq. (4).

The spring force in Eq. (5) is calculated at each Gauss integration point on the inner shell (the blastocyst). The element containing the nearest point on the outer shell (the zona pellucida) to that Gauss integration point is known from the previous time step. The element on the outer shell is approximated by a straight line and the analytical expression for the distance between a given point and a line is used to calculate $[\bar{u}_{\bar{n}}]$. If the nearest point lies outside the assumed element, the element number on the outer shell is updated and the distance to the nearest point on that updated element is calculated. The same procedure is used for the Gauss integration points on the outer shell. The sign of $[\bar{u}]_{\bar{n}}$ is the same for the inner shell (the blastocyst) and the outer shell(the zona pellucida) but the spring forces have opposite signs.

2.2. Constitutive relation

The importance of accounting for material rate dependence in modeling the mechanical response of the zone pellucida is shown in Ref. [3]. Material rate dependence is expected to play an even more important role for modeling the softer blastocyst. Here, the rate of deformation tensor, $\mathbf{d}$, in each shell is taken to be the sum of an elastic (actually hypoelastic) contribution and a linear viscous contribution so that

$$\mathbf{d} = \mathbf{d}_e + \mathbf{d}_v \tag{6}$$

where $\mathbf{d} = \text{sym}(\dot{\mathbf{F}} \cdot \mathbf{F}^{-1})$, $(\dot{})$ denotes $\partial(\ )/\partial t$ and

$$\mathbf{d}_v = \frac{1}{\mu}\boldsymbol{\tau}' \quad , \quad \mathbf{d}_e = \frac{1+\nu}{E}\hat{\boldsymbol{\tau}} - \frac{\nu}{E}\text{tr}(\hat{\boldsymbol{\tau}})\mathbf{I} \tag{7}$$

Here, $\hat{\boldsymbol{\tau}}$ is the Jaumann derivative of Kirchhoff stress, E is Young's modulus, ν is Poison's ratio, μ is the material viscosity, tr( ) denotes the trace, $\mathbf{I}$ is the second order identity tensor and

$$\boldsymbol{\tau}' = \boldsymbol{\tau} - \frac{1}{3}\text{tr}(\boldsymbol{\tau})\mathbf{I} \tag{8}$$

The elastic contribution in Eq. (7) is a hypoelastic relation in that it is not in general derivable from a strain energy function. However, for deformation histories with fixed principal axes (as in spherically symmetric expansion of a sphere) it is equivalent to a hyperelastic relation between Kirchhoff stress and logarithmic strain.

The resulting stress-rate, $\hat{\boldsymbol{\tau}}$, versus rate of deformation, $\mathbf{d}$, relation has the form

$$\hat{\boldsymbol{\tau}} = \frac{E}{1+\nu}\left[\mathbf{d} - \frac{1}{\mu}\boldsymbol{\tau}' + \frac{\nu}{1-2\nu}\text{tr}(\mathbf{d})\mathbf{I}\right] \tag{9}$$

Some calculations were carried out using a principal axis representation of a nonlinear hyperelastic relation, [9,10] (see also [11]), for the elastic contribution that is equivalent to Eq. (9) for fixed principal axes. It was found that those results differed little from those based on Eq. (9).

The reason for using Eq. (9) is that the rate form is convenient for exploring the role of large strain stiffening, namely in some calculations we specify

$$E = \begin{cases} E^a & \epsilon_{mx} \le \epsilon_s \\ E^b & \epsilon_{mx} > \epsilon_s \end{cases} \tag{10}$$

and

$$\mu = \begin{cases} \mu^a & \epsilon_{mx} \le \epsilon_s \\ \mu^b & \epsilon_{mx} > \epsilon_s \end{cases} \tag{11}$$

where ϵ_{mx} is a maximum principal strain and ϵ_s is a specified transition value.

3. Results

3.1. Spherical membrane

Spherical membrane models have been used to model a variety of biophysical processes, e.g. [4,5,12]. In particular, modeling the expansion of the blastocyst as an internally pressurized spherical membrane neglects the effects of the opening in the zona pellucida and of the constraint imposed by the zona pellucida on the stress and deformation states, but can give insight into the dependence on the constitutive response assumed for the blastocyst, e.g. [4,5]. Here, we summarize some results for a membrane that is characterized by the constitutive relation in Section 2.2.

We first consider the response of an elastic spherical membrane with constant Young's modulus $E^a = E^b = E$ and subject to internal pressure and, for simplicity, the material is taken to be incompressible so that integrating Eq (9) gives

$$\sigma_i = \frac{2}{3}E\epsilon_i + \sigma_h \tag{12}$$

where σ_i are the principal Cauchy stresses, ϵ_i are the principal logarithmic strains and σ_h is the mean normal stress, positive for hydrostatic tension.

Since $\sigma_3 = 0$ and $\epsilon_3 = -(\epsilon_1 + \epsilon_2)$, the expression for the in-membrane stresses in Eq. (12) can be written as

$$\sigma_1 = \frac{2}{3}E(2\epsilon_1 + \epsilon_2) \quad , \quad \sigma_2 = \frac{2}{3}E(2\epsilon_2 + \epsilon_1) \tag{13}$$

The state of stress in the membrane is one of equal biaxial tension so that $\epsilon_1 = \epsilon_2 = \epsilon$ and $\sigma_1 = \sigma_2 = \sigma$. The internal pressure is related to σ via

$$p = 2\frac{h}{R}\sigma \tag{14}$$

where h is the current thickness and R is the current radius. Incompressibility requires that $hR^2 = h_0R_0^2$, with h_0 and R_0 being the initial thickness and radius, respectively, so that

$$p = 2\frac{h_0}{R_0}\frac{\sigma}{\lambda^3} \tag{15}$$

where $\lambda = R/R_0 = \exp(\epsilon)$.

The pressure reaches a maximum, $\dot{p} = 0$, when $\dot{\sigma} - 3\sigma\dot{\epsilon} = 0$, so that from Eq. (13)

$$\sigma_m = \frac{2}{3}E \tag{16}$$

and $\epsilon_m = 1/3$ so that $\lambda_m^3 = \exp(1) = e$. Hence, the maximum pressure, p_m is given by

$$\frac{p_m}{E} = \frac{4}{3e}\left(\frac{h_0}{R_0}\right) \tag{17}$$

The pressure cannot exceed p_m under quasi-static loading conditions.

Bifurcation instabilities can occur after the maximum pressure but for larger values of stress if the expansion of the sphere is prescribed rather than the pressure. A long wavelength local thinning bifurcation instability mode [13] becomes possible at $\sigma = \sigma_c$ where

$$\sigma_c = \frac{3}{2}\sigma_m = E \tag{18}$$

A loss of ellipticity, [14,15], (which corresponds to an imaginary wave speed) can also occur within the plane stress context, the critical strain for equal biaxial tension at loss of ellipticity is

$\epsilon = 2/3$ from Eq. (45) of [15] with $N = 1$, so that from Eq. (13) this occurs at $\sigma = \sigma_\ell$, with

$$\sigma_\ell = \frac{4}{3}E \tag{19}$$

When material rate viscosity is accounted for and constant so that $\mu^a = \mu^b = \mu$, the constitutive relation Eq. (9) for the membrane specializes to

$$\dot{\sigma}_i = \frac{2}{3}E\left[\dot{\epsilon}_i - \frac{1}{\mu}\sigma'\right] + \dot{\sigma}_h \tag{20}$$

where μ is the viscosity. As $\mu \to \infty$, the elastic response is recovered.

An explicit expression in terms of the membrane stresses is obtained using $\dot{\sigma}_3 = 0$, $\dot{\epsilon}_3 = -(\dot{\epsilon}_1 + \dot{\epsilon}_2)$ and $\dot{\sigma}_3 = -(\dot{\sigma}_1 + \dot{\sigma}_2)$ to give

$$\begin{aligned}\dot{\sigma}_1 &= \frac{2}{3}E\left[2\dot{\epsilon}_1 + \dot{\epsilon}_2 - \frac{1}{\mu}(2\sigma_1' + \sigma_2')\right] \quad , \\ \dot{\sigma}_2 &= \frac{2}{3}E\left[2\dot{\epsilon}_2 + \dot{\epsilon}_1 - \frac{1}{\mu}(2\sigma_2' + \sigma_1')\right]\end{aligned} \tag{21}$$

For equal biaxial tension, $\sigma_1 = \sigma_2 = \sigma$, $\sigma_1' = \sigma_2' = \sigma/3$, Eq. (21) gives

$$\dot{\sigma} + \frac{1}{t_c}\sigma = 2E\dot{\epsilon} \tag{22}$$

where

$$t_c = \frac{3\mu}{2E} \tag{23}$$

The simplest case that gives qualitative insight into the effect of material viscosity is to regard the expansion rate $\dot{\epsilon} = \dot{R}/R$ as a specified constant. Then, for equal biaxial tension the solution is

$$\sigma(t) = 2E\dot{\epsilon}t_c\left[1 - \exp(-t/t_c)\right] = 3\mu\dot{\epsilon}\left[1 - \exp(-t/t_c)\right] \tag{24}$$

The maximum pressure, i.e. $\dot{p} = 0$, still occurs when $\dot{\sigma} - 3\sigma\dot{\epsilon} = 0$, which gives

$$\frac{p_m}{E} = 4\left(\frac{h_0}{R_0}\right)\left(\frac{1}{\exp(3\epsilon_m)}\right)\frac{\epsilon_m}{t_m/t_c + 3\epsilon_m} \tag{25}$$

where t_m is the time at which the pressure maximum is attained and $\epsilon_m = \dot{\epsilon}t_m = \ln(\lambda_m)$.

As $t_c \to \infty$, it can be shown that $\epsilon_m \to 1/3$ and p_m/E in Eq. (25) approaches the value in Eq. (17). As $t_c \to 0$, ϵ_m and p_m each approach zero.

For spherical expansion of a spherical membrane into an external medium with a viscosity proportional to the membrane velocity, the effective pressure acting on the membrane is the difference between the internal pressure p and the external pressure $c_m\dot{R}$, so that Eq. (15) becomes

$$p - c_m\dot{R} = 2\frac{h_0}{R_0}\frac{\sigma}{\lambda^3} \tag{26}$$

where c is the external viscous resistance. If $\dot{R}$ is constant then the condition for a maximum pressure is not affected. If $\dot{R}$ varies with time then the maximum pressure is reached when the sum of $c\ddot{R}$ and the time derivative of the right hand side of Eq. (26) vanish.

In the circumstances of interest, the soft inner shell (the blastocyst) is surrounded by the stiff outer shell (the zona pellucida). With no opening in the outer shell, expansion of the inner shell is limited by the expansion of the outer shell and the internal pressure can exceed p_m. If at some value of the internal pressure $p > p_m$, the stiff external outer shell were abruptly removed, the inner shell would tend to abruptly expand, with the rate of expansion reduced by the material viscosity, by the viscosity of the external medium and, in dynamic calculations by material inertia. The inner shell could then expand uniformly until large enough internal stresses develop to trigger an instability.

In the circumstances of interest, the predicted response is set by a complex interaction between, the material properties taken to model the blastocyst (the inner shell) and the zona pellucida (the outer shell), the rate of pressure increase, the interaction with the external medium and the size of the opening in the outer shell. The opening in the outer shell gives a possibility of relaxing stresses in the inner shell by expanding through the opening and "escaping" from the outer shell. However, for a sufficiently small opening in a sufficiently stiff outer shell, the response will approach the case of a closed outer shell. These idealized scenarios give insight into the range of responses that can be expected in the numerical solutions.

3.2. Numerical results

Numerical results are presented that illustrate some of the quantitative predictions that can be made with the modeling framework. Presuming that the material inertia term plays a minimal role (as verified computationally), there are three characteristic parameters of the boundary value problem: (i) a length scale, taken to be the inner radius R_i; (ii) a stress measure, taken to be E_i, Young's modulus of the inner shell; and (iii) a characteristic time, which using Eq. (23) as a guide, is taken to be $t_i = 3\mu_i^a/2E_i^a$. If all lengths are normalized with R_i, all stress measures with E_i and all times with t_i, the governing equations (with the inertia term deleted) are in non-dimensional form and therefore so are the results. For example, the normalized viscosity of the external medium is $c_N = c_d R_i^2/(E_i t_i)$ where c_d is the prescribed viscosity.

The finite element implementation follows that in [7] where additional details and references are given. The finite element discretization of Eq. (2) uses eight node quadratic displacement elements with four point Gauss integration for the force term in each element and nine point Gauss integration for the viscous force and mass terms in each element. The pressure surface integral is calculated using four Gauss points along each surface element whereas the spring force term along $R = R_s$ is evaluated using three point Gauss integration. Explicit time integration is carried out using a Newmark-β method with $\gamma = 1/2$ and $\beta = 0$.

The fixed parameters in the results to be presented are $R_s/R_i = 1.2$, $R_o/R_i = 1.4$, $E_o^a/E_i^a = 4.286$, $E_o^b/E_o^a = 1.0$, $\mu_o^b/\mu_o^a = 1.0$, and $\dot{p}t_i/E_i = 0.375 \times 10^{-3}$. The normalized density in all calculations was taken to be $\rho_N = \rho_d R_i^2/(Et_i^2) = 9.14 \times 10^{-3}$ where ρ_d is the prescribed density.

The finite element mesh used in the calculations has 5 elements across the inner shell (the blastocyst) $R_i \le r \le R_s$, 5 elements across the outer shell (the zona pellucida) $R_s \le r \le R_o$ and 92 elements along $-90^\circ \le \phi \le 90^\circ$.

The presumption that the material inertia term plays a minimal role in the computations was tested by carrying out a calculation with the inertia term set to zero and using an explicit Euler time stepping scheme. The predicted pressure–volume response and the predicted evolution of the deformed blastocyst/zona pellucida structure were nearly identical to those obtained from the full dynamic calculation even though in the latter stages of the full dynamic calculation the kinetic energy was up to 6% of the stress work; for example, the calculation with the inertia term set to zero reached $V/V_0 = 16$ at $p/E_i^a = 0.0134$ whereas the reference calculation reached $V/V_0 = 16$ at $p/E_i^a = 0.0136$. However, the time step required for numerical stability for the calculation with the inertia term set to zero was a factor of about 500 smaller than the time step that could be used for the full dynamic calculations. With inertia neglected, an implicit

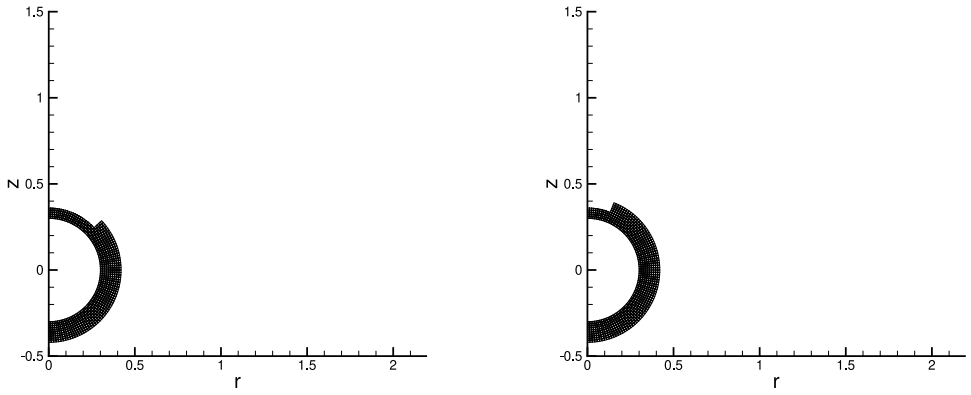

Fig. 2. Initial finite element meshes. (a) 24 elements in the opening so that $\theta_0 = 47.0°$. (b) 11 elements in the opening so that $\theta_0 = 21.5°$.

time stepping scheme could be used that would allow much larger time steps over much of the deformation history. However, convergence of such iterations can be problematic when a rapid change in stress state and/or deformation state takes place (as occurs in most calculations here) unless the time step is taken to be very small. Furthermore, an iterative approach is more complex to code and so was not pursued here.

Results are presented for four calculations with $\theta_0 = 47.0°$ as in Fig. 2a (there are 24 elements in the opening), and $\mu_o^a/\mu_i^a = 8.0$ so that the characteristic time associated with the outer shell is $3\mu_o^a/2E_o^a = 1.87t_i$. The normalized stiffness of the springs along $R = R_s$ is taken to be $KR_i/\delta_n E_i = 3.0$. In two of the calculations $c = 0$ while in the other two calculations $c = c_N = c_d R_i^2/(E_i t_i) = 0.0343$.

The four calculations with $\theta_0 = 47.0°$, are specified by:

Case 1: $e_R = E_i^b/E_i^a = 1$, $\mu_R = \mu_i^b/\mu_i^a = 1$, $c = 0$.
Case 2: $e_R = E_i^b/E_i^a = 1$, $\mu_R = \mu_i^b/\mu_i^a = 1$, $c = c_N$.
Case 3: $e_R = E_i^b/E_i^a = 3$, $\mu_R = \mu_i^b/\mu_i^a = 32$ with $\epsilon_s = 0.90$, $c = 0$.
Case 4: $e_R = E_i^b/E_i^a = 3$, $\mu_R = \mu_i^b/\mu_i^a = 32$ with $\epsilon_s = 0.90$, $c = c_N$.

The evolution of the enclosed volume versus pressure for these four cases is shown in Fig. 3. The pressure–volume response for all four cases is essentially the same until $p/E_i^a \approx 0.0125$. Consistent with the membrane expression Eq. (26) the external medium viscosity delays expansion but the magnitude of the effect depends on the constitutive characterization of the inner shell (the blastocyst). The external medium viscosity (with $c_N = 0.0343$) has only a small effect on the response when $e_R = \mu_R = 1$ but has a large effect on the response when $e_R = 3$, $\mu_R = 32$. When $e_R = \mu_R = 1$, the enclosed volume increases rapidly at nearly constant pressure of $p/E_i^a \approx 0.014$, much like expected when a maximum pressure is attained. For a membrane with the material properties (E_i^a, μ_i^a) and the thickness to mean radius ratio of the inner shell, and estimating $\dot{\epsilon} \propto \dot{p}$ at small strains, Eq. (25) gives $p_m/E_i^a \approx 0.004$. For an elastic membrane with the same thickness to mean radius ratio $p_m/E_i^a \approx 0.09$ from Eq. (17), which shows the large effect of material viscosity on the pressure–volume response. The pressure at which the rapid enclosed volume change occurs in Fig. 3 is greater than the membrane value from Eq. (25) for two reasons: (i) the constraint on expansion imposed by the outer shell; and (ii) the membrane approximation underestimates the pressure needed to attain a given enclosed volume for a finite thickness shell. An axisymmetric finite element solution for an unconstrained inner shell gives $p_m/E \approx 0.012$ so that for $\theta_0 = 47.0°$, reason (ii) most likely dominates.

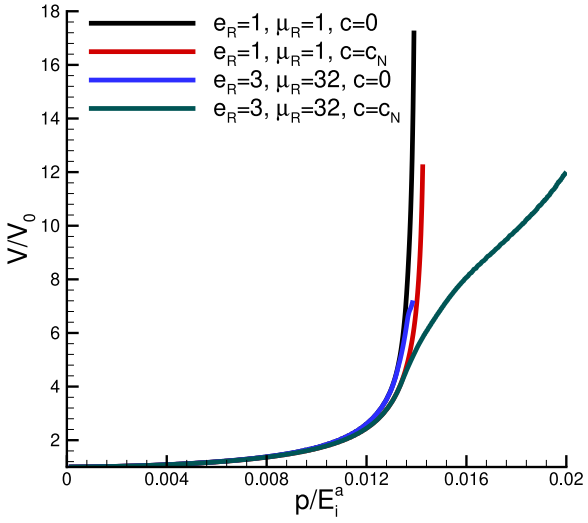

Fig. 3. Volume expansion, V/V_0 versus normalized pressure, p/E_i^a, for four cases with $\theta_0 = 47.0°$. The linear calculations are carried out with $e_R = E_i^b/E_i^a = 1$ and $\mu_R = \mu_i^b/\mu_i^a = 1$ while the nonlinear calculations have $e_R = E_i^b/E_i^a = 3$ and $\mu_R = \mu_i^b/\mu_i^a = 32$. Two calculations have $c = 0$ and two have $c = c_N = 0.0343$. All other parameters are the same for all four calculations and are given in the text.

For all four cases in Fig. 3 until $p/E_i^a \approx 0.0125$ the inner shell expands but does not separate from the outer shell. This is shown for case 1, $e_R = 1$, $\mu_R = 1$ and $c_N = 0$, in Fig. 4a. As the pressure continues to increase, the bulging increases until the inner shell begins to separate from the outer shell and the enclosed volume increases at a nearly constant pressure. For case 1, the hatching process is essentially complete at $p/E_i^a = 0.0135$, as shown in Fig. 4b. Regarding the inner shell as a spherical membrane of uniform thickness and estimating the average stress in the blastocyst from Eq. (14) gives $\sigma/E_i^a = 0.24$. However, the stress distribution in the inner shell (the blastocyst) is not uniform and locally the stress magnitude can be larger.

The stress in the inner shell increases rapidly as expansion increases and the calculation becomes numerically unstable shortly after the deformation stage shown in Fig. 4b. Such a numerical instability eventually occurs in all calculations here and is associated with the magnitude of the maximum principal stress in the inner shell becoming equal to or larger than the value of Young's modulus. One possibility is that such a large stress level induces a mechanical instability as noted in Section 3.1 for a membrane but

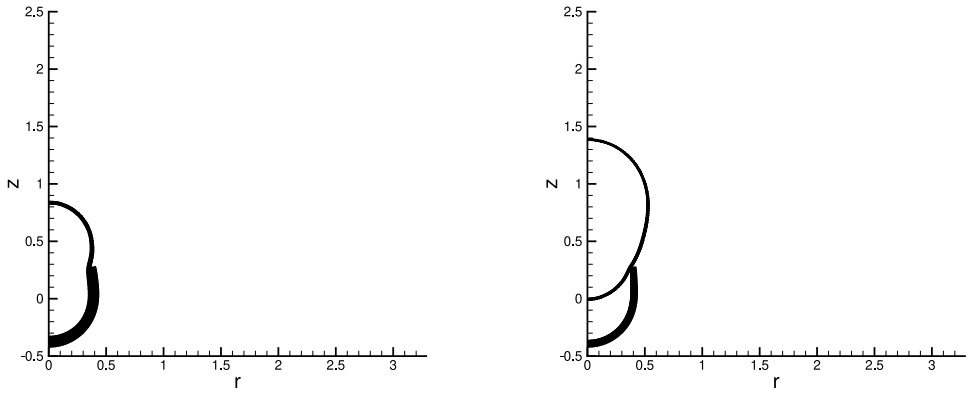

Fig. 4. Deformed configurations for case 1, the calculation with $\theta_0 = 47.0°$, $E_i^b/E_i^a = 1$, $\mu_i^b/\mu_i^a = 1$ and $c = 0$. (a) $V/V_0 = 3.09$, $p/E_i^a = 0.0125$, $t/t_i = 33.3$. (b) $V/V_0 = 6.67$, $p/E_i^a = 0.0135$, $t/t_i = 36.1$.

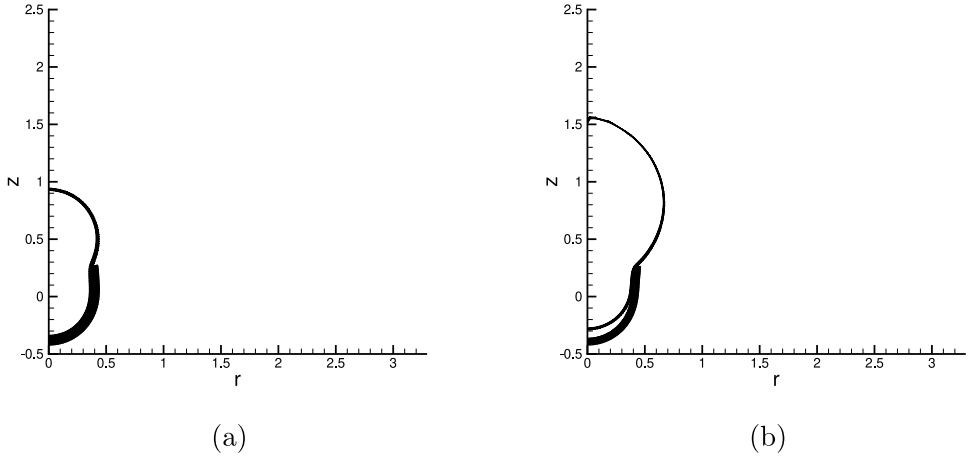

Fig. 5. Deformed configurations for case 2, the calculation with $\theta_0 = 47.0°$, $E_i^b/E_i^a = 1$, $\mu_i^b/\mu_i^a = 1$ and $c = c_N$. (a) $V/V_0 = 4.00$, $p/E_i^a = 0.0133$, $t/t_i = 35.5$. (b) $V/V_0 = 12.3$, $p/E_i^a = 0.0143$, $t/t_i = 38.0$.

a similar mechanical instability occurs in the context of a three dimensional framework, [14,16]. Another possibility is that the large mesh distortions associated with the large stresses induce a numerical instability before the mechanical instability occurs. Whether or not the instability that occurs in the calculations here is induced by the mesh distortions or is a consequence of a mechanical instability cannot be decided based solely on numerical calculations. It is worth noting that large stresses occurred in the exploratory calculations where inertia was neglected and where the constraint $[\bar{u}]_{\bar{n}} = 0$ was enforced on part of the interface.

An external medium viscosity value of $c_N = 0.0343$ leads to increased stress and strain levels in the inner shell. Using Eq. (14) to estimate the average stress level in the configuration in Fig. 5b gives $\sigma/E_i^a = 0.37$. For the nonuniform stress distribution, the maximum principal Kirchhoff stress at each Gauss integration point can be calculated[1] At $p/E_i^a = 0.0133$, Fig. 5a, the configuration is nearly the same as for the calculation with $c = 0$ in Fig. 4a. However, shortly after the state shown in Fig. 5b where $p/E_i^a = 0.0143$, a maximum principal stress value greater than E_i^a is attained locally at the intersection of the inner shell with the z-axis and the calculation becomes numerically unstable. The external medium viscosity has two competing effects: from Eq. (26) it tends to reduce the effective pressure acting on the inner shell; on the other hand, when expansion is constrained (by the outer shell), it leads to an increased stress magnitude.

Fig. 6 shows two stages of deformation for case 3. The viscosity of the external medium is neglected, as in case 1, but the stiffness of the inner shell increases when the maximum principal strain exceeds 0.90. Compared with case 1, where $E_i/E_i^a = 1$ and $\mu_i/\mu_i^a = 1$ for all values of strain, the rate of volume expansion is reduced once the inner shell begins to escape from the outer shell. For example, at $p/E_i^a = 0.01382$, the increased deformation resistance at large strains reduces $V/V_0 = 12.2$ for case 1 to $V/V_0 = 7.1$ for case 3. Even though $E_i^b/E_i^a = 3$, at large values of V/V_0, a maximum principal stress value equal to or greater than E_i^b is attained and the calculation for case 3 eventually terminates due to a numerical instability.

A more detailed picture of the evolution of the deformation history is shown for case 4($e_R = 3$, $\mu_R = 32$ and $c_N = 0.0343$) in Fig. 7 where four configurations are shown. At $t/t_i = 28.9$ in Fig. 7a the inner shell has bulged out a bit through the opening but there is relatively little expansion of the outer shell and, except for the bulging, the deformation of the rest of the shell is nearly spherically symmetric. At the somewhat later time $t/t_i = 35.5$ in Fig. 7b, the bulging has increased considerably and the increased pressure has led to a larger opening of the outer shell. Relatively shortly after this, Fig. 7c, the two shells begin to separate and the hatching process is essentially complete at

[1] Since both the inner shell and the outer shell materials are taken to be nearly incompressible, Kirchhoff stress values and Cauchy stress values are nearly equal.

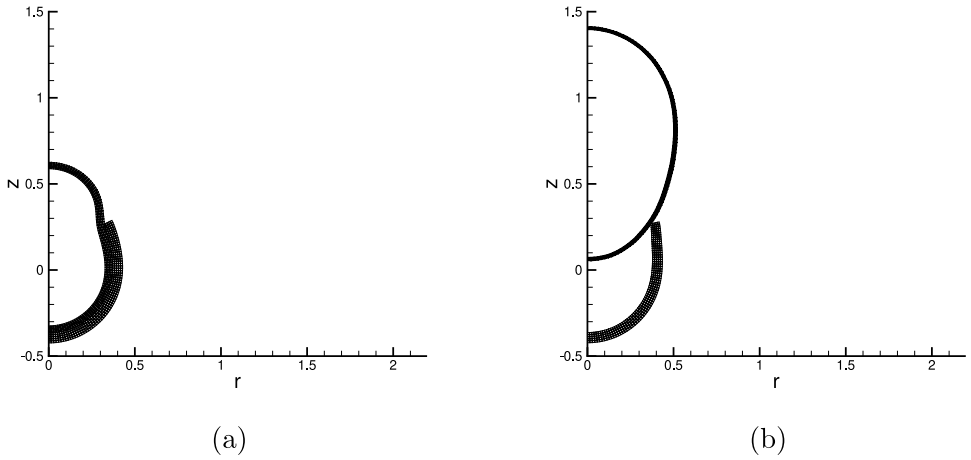

Fig. 6. Deformed configurations for case 3, the calculation with $\theta_0 = 47.0°$, $E_i^b/E_i^a = 3$, $\mu_i^b/\mu_i^a = 32$ and $c = 0$. (a) $V/V_0 = 1.83$, $p/E_i^a = 0.0104$, $t/t_i = 27.7$. (b) $V/V_0 = 6.21$, $p/E_i^a = 0.0136$, $t/t_i = 36.2$.

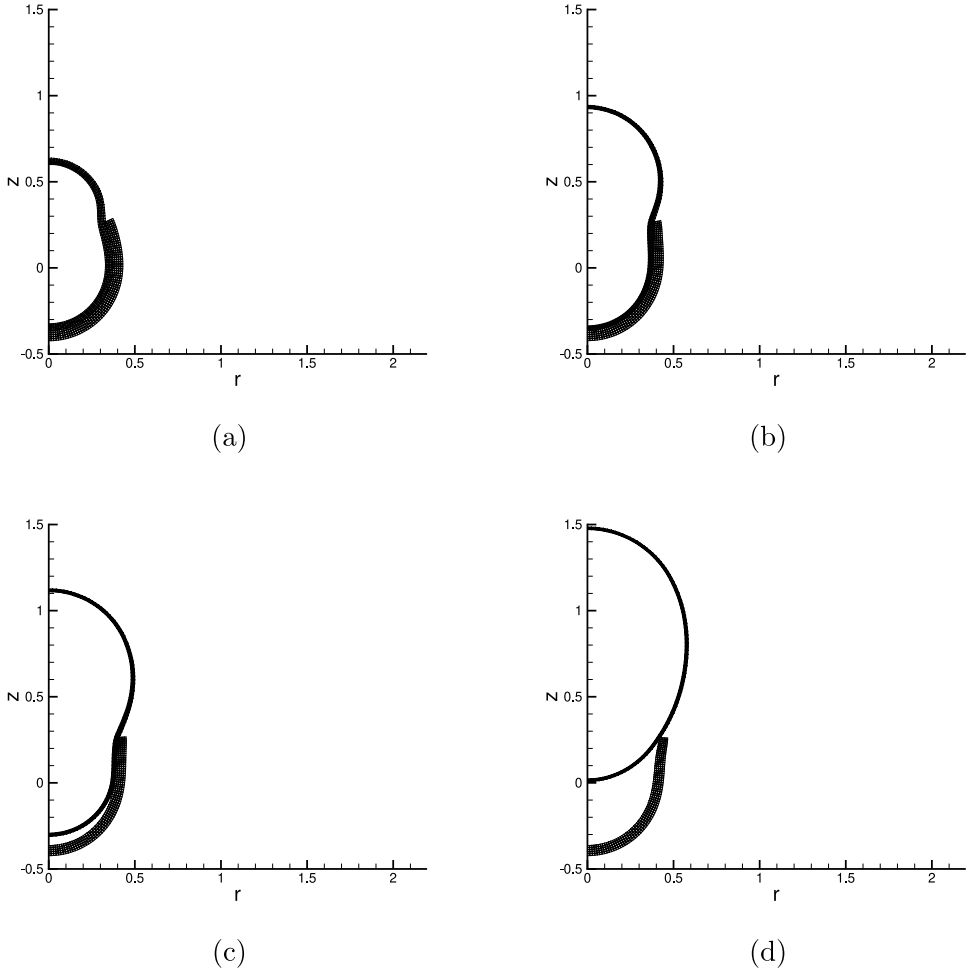

Fig. 7. Deformed configurations for case 4, the calculation with $\theta_0 = 47.0°$, $E_i^b/E_i^a = 3$, $\mu_i^b/\mu_i^a = 32$ and $c = c_N$. (a) $V/V_0 = 1.91$, $p/E_i^a = 0.0108$, $t/t_i = 28.9$. (b) $V/V_0 = 3.99$, $p/E_i^a = 0.0133$, $t/t_i = 35.5$. (c) $V/V_0 = 5.68$, $p/E_i^a = 0.0142$, $t/t_i = 37.8$. (d) $V/V_0 = 8.68$, $p/E_i^a = 0.0167$, $t/t_i = 44.4$.

$t/t_i = 44.4$ in Fig. 7d. The time interval from the initiation of separation until complete separation is about 18% of the time interval from $t/t_i = 0$ to $t/t_i = 44.4$.

Comparing the results for cases 1 and 2 with those for cases 3 and 4 shows that the effect of the external medium viscosity depends on the constitutive characterization of the inner shell. For a "soft" inner shell as for cases 1 and 2, the viscosity of the external medium retards separation of the two shells and leads to high stresses in the inner shell. When the inner shell stiffens, as in cases 3 and 4, separation is favored over constrained expansion. Once the inner shell starts to escape, the viscosity of the external medium reduces the effective pressure and a slow expansion continues.

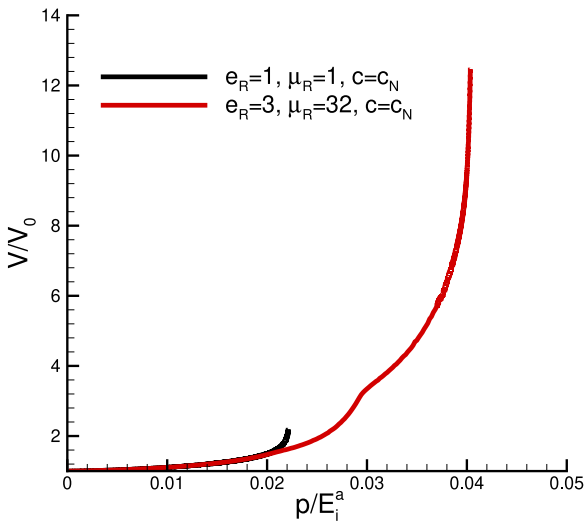

Fig. 8. Volume expansion, V/V_0 versus normalized pressure, p/E_i^a, for two shells with $\theta_0 = 21.5°$ and $c = c_N = 0.0343$. The linear calculations are carried out with $e_R = E_i^b/E_i^a = 1$ and $\mu_R = \mu_i^b/\mu_i^a = 1$ while the nonlinear calculations have $e_R = E_i^b/E_i^a = 3$ and $\mu_R = \mu_i^b/\mu_i^a = 32$. All other parameters are the same for the two calculations and are given in the text.

Fig. 8 shows the pressure volume response for two calculations with $\theta_0 = 24.5°$ as in Fig. 2b (the opening consists of 11 elements), $\mu_o^a/\mu_i^a = 32$ and the normalized spring stiffness is $KR_i/\delta_n E_i = 6.0$ (all other parameters are the same as for the calculations with $\theta_0 = 47.0°$). In both calculations $c = c_N = 0.0343$. The pressure at which the enclosed volume rapidly increases is much greater than for the shells with $\theta_0 = 47.0°$ due to the increased constraint. A pressure of $p/E_i^a = 0.02$ is greater than reached in any calculation shown in Fig. 3. For $\theta_0 = 24.5°$ the difference between the maximum pressures attained in Fig. 8 and that for an unconstrained shell is likely mainly due to the constraint provided by the outer shell.

Two stages of deformation are shown in Fig. 9 for an inner shell with $E_i^b/E_i^a = 1$ and $\mu_i^b/\mu_i^a = 1$. As a consequence of the increased stress level arising from the stronger constraint the stress magnitudes become very large (relative to $E_i^b = E_i^a$) and a numerical instability occurs in an early stage of bulging prior to any separation.

Stiffening of the inner shell at large strains leads to a very different deformation history as shown in Fig. 10. At an early stage of deformation, Fig. 10a, the deformation mode is much like that in Fig. 9b. The numerical instability is delayed due to the increased stiffness at large strains and separation is beginning at the stage shown in Fig. 10c. Escape is nearly complete in Fig. 10d.

Fig. 11 shows contours of the maximum principal Kirchhoff stress, τ_1, in the configuration shown in Fig. 10d. Although details of the stress distribution cannot be seen because the shells are thin, this plot shows that: (i) the stress distribution in the inner shell (the blastocyst) is nonuniform; (ii) that the stresses are relaxed in the outer shell (the zona pellucida) as the inner shell escapes and (iii) the maximum principal stress magnitude over a significant region of the inner shell is of the order of E_i^b. Shortly after the stage of deformation shown in Fig. 11, $\tau_1 > E_i^b$ in the inner shell and the calculation becomes numerically unstable.

At the stage in Fig. 10c $t/t_i = 103.9$, while in Fig. 10d is $t/t_i = 107.6$. Thus, the time interval over which escape occurs with $\theta_0 = 24.5°$ is about 4% of the total time interval as compared with 18% when $\theta_0 = 47.0°$. Thus, after a relatively long, opening-size dependent, period of bulging the inner shell "pops" out. This is qualitatively consistent with the observation in Ref. [17] that once a blastocyst hatches out more than halfway the embryo emerges rather quickly and then expands rapidly.

To illustrate the predicted time for hatching, we set $t_i^a = 3\mu_i^a/2E_i^a = 20$min, which if we take $E_i^a = 7$KPa corresponds to $\mu_i^a = 93.3$KPa-min. Then, separation of the inner shell (the blastocyst) in Fig. 7d where $\theta_0 = 47.0°$ occurs in 14.8 h whereas for the case with $\theta_0 = 24.5°$ in Fig. 10d separation occurs in 35.8 h. This illustrates the strong effect of the opening size and of the deformation resistance of the outer shell (the zona pellucida) on the time for hatching.

4. Concluding remarks

We have developed a continuum mechanics modeling framework for simulating the hatching of a blastocyst from the zona pellucida. Calculations carried out within that framework reproduce, at least qualitatively, some features observed experimentally, such as hatching consisting of a long time period where part of the blastocyst bulges out of the opening in the zona pellucida prior to hatching. While simplified, our modeling framework can predict trends for the dependence of hatching on geometrical and material parameters as well as make quantitative predictions for specific cases. Hopefully, these will be helpful for developing a predictive theory of the mechanics of hatching. For example, our model can make qualitative and quantitative predictions of the

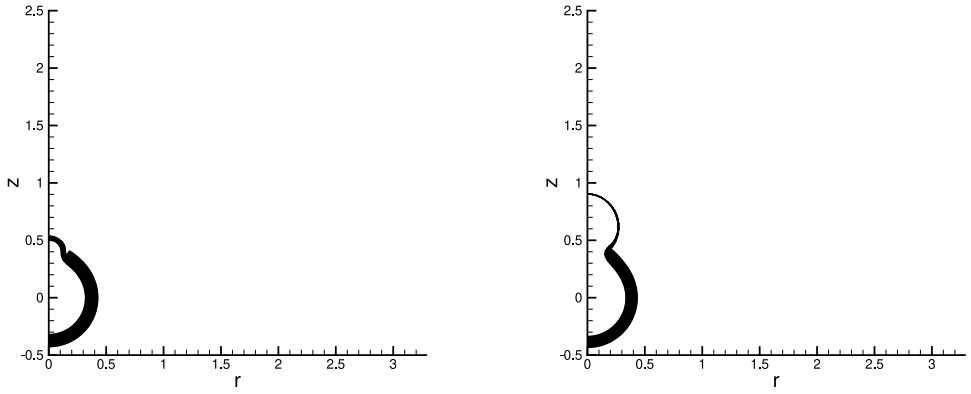

Fig. 9. Deformed configurations for the calculation with $\theta_0 = 24.5°$, $E_i^b/E_i^a = 1$, $\mu_i^b/\mu_i^a = 1$ and $c = c_N$. (a) $V/V_0 = 1.28$, $p/E_i^a = 0.0164$, $t/t_i = 43.7$. (b) $V/V_0 = 2.16$, $p/E_i^a = 0.0221$, $t/t_i = 59.0$.

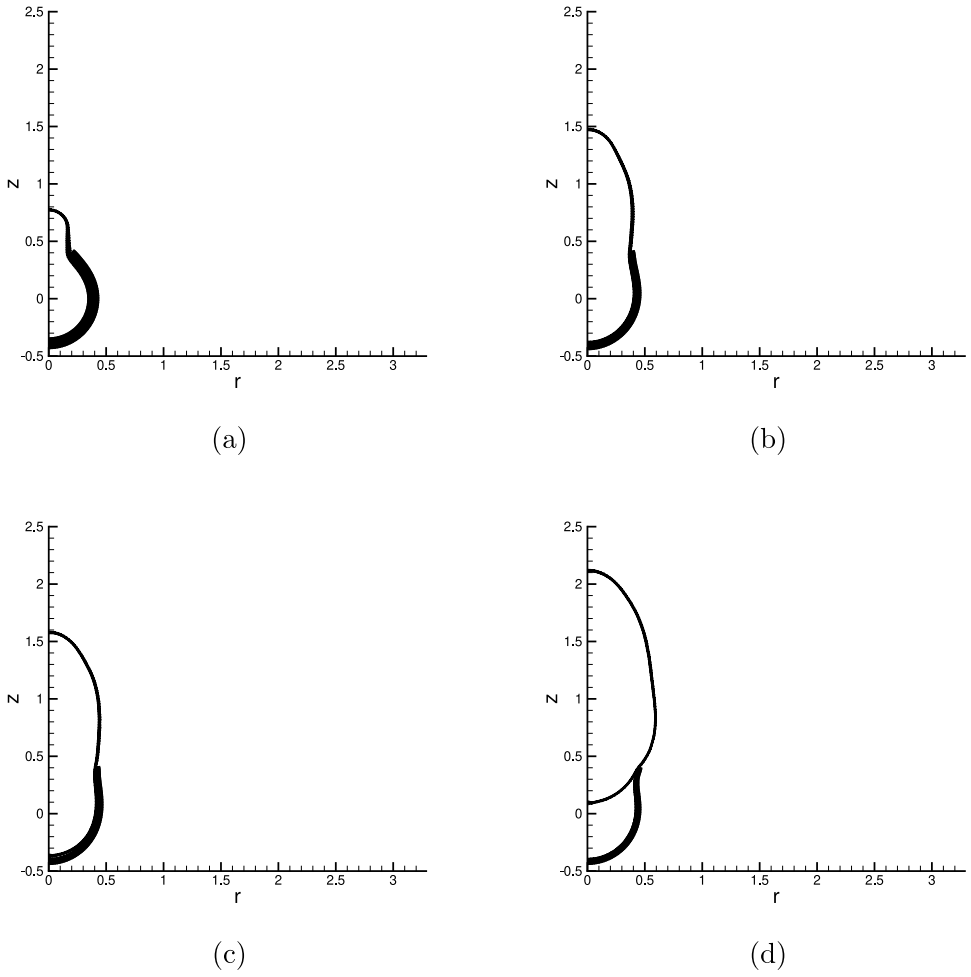

Fig. 10. Deformed configurations for the calculation with $\theta_0 = 24.5°$, $E_i^b/E_i^a = 3$, $\mu_i^b/\mu_i^a = 32$ and $c = c_N$. (a) $V/V_0 = 1.75$, $p/E_i^a = 0.0235$, $t/t_i = 62.7$. (b) $V/V_0 = 5.80$, $p/E_i^a = 0.0371$, $t/t_i = 99.0$. (c) $V/V_0 = 7.33$, $p/E_i^a = 0.0390$, $t/t_i = 103.9$. (d) $V/V_0 = 12.40$, $p/E_i^a = 0.0403$, $t/t_i = 107.6$.

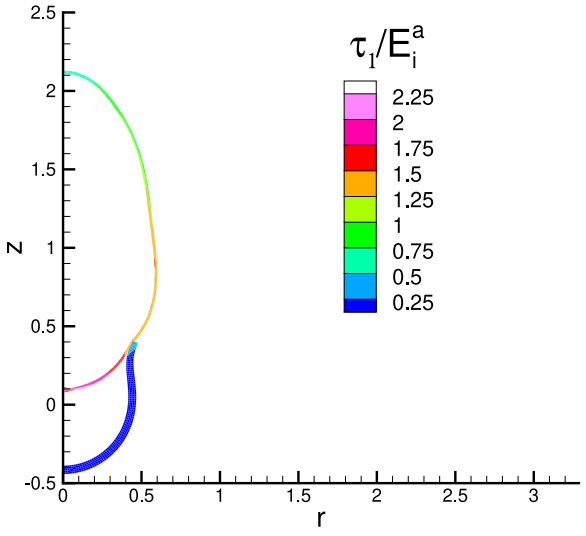

Fig. 11. Distribution of maximum principal Kirchhoff stress τ_1 in the deformed configuration for the calculation with $\theta_0 = 24.5°$, $E_i^b/E_i^a = 3$, $\mu_i^b/\mu_i^a = 32$ and $c = c_N$ at $V/V_0 = 12.40$, $p/E_i^a = 0.0403$, $t/t_i = 107.6$.

dependence of the time evolution of the hatching process, including whether or not hatching is successful, on the size of the zona pellucida opening and on the constitutive characterization of the blastocyst and of the zona pellucida. The results presented here show a strong effect of material nonlinearity on the predicted hatching process. Also, the evolution of the shape and thickness of both the blastocyst and the zona pellucida is predicted.

In our model the constraint of the outer shell (the zona pellucida) significantly increases stress levels in the inner shell (the blastocyst), as was also suggested in Ref. [4]. This constraint, coupled with the opening in the outer shell, leads to a non-uniform stress distribution in the inner shell. This contrasts with a blastocyst membrane model that gives a uniform stress distribution. The stress distribution could be important for understanding the evolution of cell shape and size in the blastocyst. Our results illustrate predictions for the dependence of the stress levels attained on the constitutive characterization of the inner shell and of the outer shell as well as on the viscosity of the surrounding medium and on the size of the opening in the outer shell.

The observed response of the blastocyst typically displays cycles of expansion and collapse, see for example [4,18], the possibility of which is not included in the constitutive description used in our calculations. However, the large local stresses that occur in our calculations could induce cell separation which could in turn initiate collapse. A multi-axial constitutive description incorporating cyclic collapse and expansion could be incorporated into our framework.

An important aspect of our modeling framework is that it is extensible. Improved constitutive descriptions, an improved

model of the interface between the blastocyst and the zona pellucida, and an improved model of the interaction between the blastocyst/zona pellucida structure with the surrounding viscous medium can be incorporated. Also, we have presumed that the opening is fixed during the hatching process. An evolution equation for the development of the opening during hatching could be incorporated. A quantitative experimental characterization of the deformation history during hatching is needed to assess the predictive capability of the modeling and to identify the key features of the model that need to be improved.

Declaration of competing interest

The authors declare that they have no known competing financial interests or personal relationships that could have appeared to influence the work reported in this paper.

References

[1] F. Sinowatz, E. Topfer-Peterson, S. Kolle, G. Palma, Functional morphology of the zona pellucida, Anat. Histol. Embryol. 30 (2001) 257–263.
[2] M. Papi, R. Brunelli, L. Sylla, T. Parasassi, M. Monaci, G. Maulucci, M. Missori, G. Arcovito, F. Ursini, M. De Spirito, Mechanical properties of zona pellucida hardening, Eur. Biophys. J. 39 (2010) 987–992.
[3] M. Papi, A. Maiorana, C. Douet, G. Maulucci, T. Parasassi, R. Brunelli, G. Goudet, M. De Spirito, Viscous forces are predominant in the zona pellucida mechanical resistance, Appl. Phys. Lett. 102 (2013) 043703.
[4] C.J. Chan, M. Costanzo, T. Ruiz-Herrero, G. Mönke, R.J. Petrie, M. Bergert, A. Diz-Muñoz, L. Mahadevan, T. Hiiragi, Hydraulic control of mammalian embryo size and cell fate, Nature 571 (2019) 112–116.
[5] K. Leonavicius, C. Royer, C. Preece, B. Davies, J.S. Biggins, S. Srinivas, Mechanics of mouse blastocyst hatching revealed by a hydrogel-based microdeformation assay, Proc. Natl. Acad. Sci. 115 (2018) 10375-10380.
[6] Cohen J., Assisted hatching of embryos, J. In Vitro Fert. Embryo Transf. 8 (1991) 179–190.
[7] B. Lindgreen, V. Tvergaard, A. Needleman, Dynamic neck development in a polymer tube under internal pressure loading, Int. J. Solids Struct. 45 (2008) 580–592.
[8] V. Tvergaard, A. Needleman, Indentation of pressurized viscoplastic polymer spherical shells, J. Mech. Phys. Solids 93 (2016) 16–33.
[9] R. Hill, Constitutive inequalities for isotropic elastic solids under finite strain, Proc. R. Soc. Lond. Ser. A Math. Phys. Eng. Sci. 314 (1970) 457–472.
[10] R. Hill, Aspects of invariance in solid mechanics, in: C.-S. Yih (Ed.), Advances in Applied Mechanics, Vol. 18, Academic Press, New York, NY, 1978, pp. 1–75.
[11] V. Tvergaard, A. Needleman, K.K. Lo, Flow localization in the plane strain tensile test, J. Mech. Phys. Solids 29 (1981) 115–142.
[12] H. Turlier, B. Audoly, J. Prost, J.-F. Joanny, Furrow constriction in animal cell cytokinesis, Biophys. J. 106 (2014) 114–123.
[13] A. Needleman, Inflation of spherical rubber balloons, Int. J. Solids Struct. 13 (1977) 409–421.
[14] J. Hadamard, Lecons sur la Propagation des Ondes et les Equations de L'Hydrodynaroique, Paris, Chp. 6, 1903.
[15] S. Stören, J.R. Rice, Localized necking in thin sheets, J. Mech. Phys. Solids 23 (1975) 421–441.
[16] J.R. Rice, The localization of plastic deformation, in: W.T. Koiter (Ed.), Proc. 14th Int. Congr. Theoret. Appl. Mech., North- Holland, 1977, pp. 207–220.
[17] H. Sathananthan, J. Menezes, S. Gunasheela, Mechanics of human blastocyst hatching in vitro, Reprod. BioMed. Online 7 (2003) 228–234.
[18] R.A. Shafeia, A.G. Syrkashevab, A.Y. Romanovb, N.P. Makarovab, N.V. Dolgushinab, M.L. Semenovaa, Blastocyst hatching in humans, Russ. J. Dev. Biol. 48 (2017) 5–15.